Journal of The Electrochemical Society

Understanding the Performance Increase of Catalysts Supported on N-Functionalized Carbon in PEMFC Catalyst Layers

Journal of The Electrochemical Society, 2022 **169** 054520

Understanding the Performance Increase of Catalysts Supported on N-Functionalized Carbon in PEMFC Catalyst Layers

Sebastian Ott,[1] Fengmin Du,[2] Mauricio Lopez Luna,[3] Tuan Anh Dao,[2] Beatriz Roldan Cuenya,[3] Alin Orfanidi,[2,z] and Peter Strasser[1,z]

[1]*Department of Chemistry, Chemical Engineering Division, Technical University of Berlin, Berlin, Germany*
[2]*BMW Group, 80788 Munich, Germany*
[3]*Department of Interface Science, Fritz Haber Institute of the Max Planck Society, 14195, Berlin*

Applying nitrogen-modified carbon support in PEMFCs has been attracting arising interest due to the resulting performance enhancement. In the present study, we attempt to uncover the origin and gain a deeper understanding of the different N-modification processes, whose influences are responsible for the performance improvement. By utilizing chemically modified Ketjenblack supports comprising altered fraction of N-functionalities, we investigate the underlying mechanism of the drastically reduced voltage losses under fuel cell operation conditions. In all, we demonstrate the key role of support modification induced by ammonia in strengthened support/ionomer interactions and alter physico-chemical properties of the carbon support contributing towards enhanced MEA performance. With the use of X-ray photoelectron spectroscopy (XPS), we show unambiguous evidences that not all N modified surfaces yield the desired performance increase. Rather, the latter depends on a complex interplay between different electrochemical parameter and catalyst properties. We want to emphasize the ionomer/support interaction as one important factor for enhanced ionomer distribution and present a prove of a direct interaction between the ionomers´ sidechains and N-functional groups of the support.

 [DOI: 10.1149/1945-7111/ac6e4d]

Manuscript submitted July 12, 2021; revised manuscript received February 23, 2022. Published May 23, 2022.

Supplementary material for this article is available online

Polymer electrolyte membrane fuel cells (PEMFCs), being currently in use in automotive and stationary applications, provide high potential for future sustainable economy and infrastructure.[1] Nevertheless, their wide commercial spread is still hindered by their relatively high production costs. One of the major reasons is the sluggish kinetics of the oxygen reduction reaction (ORR) on the PEMFC cathode, which translates into the requirement of high amount of catalytic noble metal such as Pt.[2,3] To meet the automotive cost targets, it has been shown that the loading of Pt would need to be reduced to 5 g per vehicle.[4] While the state-of-the-art Pt loading is around 0.3 mg_{Pt} cm^{-2} on the cathode, different attempts and achievements have been made to reduce it to below 0.1 mg_{Pt} cm^{-2} without sacrificing in fuel cell performance.[1–3,5,6] It is vital that the Pt based catalysts are supported on high surface area carbons ($> 800\ m^2 g^{-1}$), which enables an increased mass activity compared to low surface area ones.[3] The high mass activity of the catalyst ensures a high PEMFC performance under low current densities, which corresponds to the low power requirements of the fuel cell electric vehicles (FCEVs) and is one of the critical aspects regarding to the operating strategy of automotive fuel cell stacks.[7]

On the other hand, to cover the entire operating range of a fuel cell, high current density performance plays a deciding role. Under high current load, oxygen depletion occurs on the surface of the catalyst active sites. Over the last years, several breakthroughs have been made in fuel cell catalyst development, with several critical features towards performance improvement being identified. There is a lively discussion of which factor is limiting the high current performance the mostly. For instance, the electrochemical surface area (ECSA) plays a critical role, since it determines the number of active sites per active area and thus the local flux of the oxygen molecules.[8] At the same time, oxygen transport is influenced by the ionomer configuration, since O_2 molecules have to diffuse through the ionomer layer to reach the catalyst active sites.[2] It is known that catalyst design parameters, especially the location of the Pt particles, influence both the ECSA and the mass transport to a great extent. A higher fraction of external Pt particles (on the surface of the carbon primary particles) results in better mass transport, yet leads to decreased mass activity due to more adsorption and poisoning effect of the ionomer.[7,9,10] Proton conductive pathway was also identified as one additional key aspect based on the fact that the reduction of each O_2 molecule requires four protons. The quality of such pathway is mainly determined by the ionomer distribution within the cathode catalyst layer (CL), where a poorly designed one leads to significant ohmic losses under high current densities, especially under reduced humidity conditions.[11] Some researcher, in contrary, claimed that the physical properties of the catalyst support, e.g. its porosity, pore accessibility and hydrophobicity, play a more dominating role in limiting the high current performances.[3,7,10] The presence of multiple influential factors as mentioned complicates their characterizations during fuel cell operation as well as further developments of the CL towards performance optimization. A lot of effort has been made to improve the activity of the active sites by shape-controlled approaches, dealloying etc.[7,12–15]

Nonetheless, little attention has been paid so far for the effects of the carbon surface properties and their contribution towards performance enhancement. Orfanidi et al. accomplished significant improvement in catalyst performance at high current densities, by introducing N-functional groups into the lattice of the carbon support.[5,16] The mechanism was claimed to be the Coulombic interaction between the ionomer sidechains ($-SO_3^-$) and the positively charged N-moieties.[17,18] During the electrode manufacturing process, this interaction results in a more homogenous ionomer distribution. Such N-functionalities appear to be one parameter affecting the catalyst/ionomer interaction and the resulting performance. Nevertheless it is a very complex interplay and many different parameters are determining.[19] The characteristics of the ionomer sidechains itself play a crucial role since the length and the ether-/terminal sulfonate- groups tend to directly interact with the catalyst what appears to be even more pronounced with a high degree of ionomer flexibility.[20] Furthermore the pore structure of the support material and the final catalyst layer are major factors in matter of support/ionomer interaction, mass transport issues and water management. Hereby the pore opening corelates with the accessibility of the active sites whereas the micropore and macropore volume of the support material appear to directly influence the

[z]E-mail: alin.orfanidi@bmw.de; pstrasser@tu-berlin.de

local oxygen resistance and proton resistance, respectively.[10,21,22] Within the CL the pore size distribution is non-depending on the layer thickness whereas the porosity itself does. Two effects of the CL porosity come into account, a low one is associated with increased oxygen mass transport resistance and a high one in turn favors flooding.[23] Herein we revisited the beneficial effects of carbon surface functionalization in a very recent study, where we utilized an N-functionalized carbon support and demonstrated that the interaction of N groups and ionomer seems to facilitate a more homogenous distribution of the ionomer film over the entire CL.[16] The homogeneity of the ionomer coverage has been shown to possess the advantage of providing a steady proton pathway throughout the CL, alongside with minimized oxygen mass transport resistances. At the same time, the ECSA is maximized due to the optimal accessibility of the Pt particles. Furthermore, water management in the CL is improved, since the produced water is dispersed more evenly through a homogenous ionomer film. All experiments to date point to the fact that the carbon support/ionomer interaction affects the ionomer distribution,[24] which, in turn, controls critical transport factors and contributes favorably to the power performance of a PEMFC. Despite these advances, fundamental insights in the nature of the carbon/ionomer interactions as well as their effect at varying relative humidity were missing. This study is to meet this knowledge gap.

Here, we investigate the chemical nature of the carbon/ionomer interactions of N doped catalyst supports in PEMFCs under dry and wet conditions. In particular, carbons supports were functionalized in NH_3 under different heat treatment temperatures, resulting in alteration of the physicochemical characteristics of the N modified supports. We seek a fundamental understanding of the interaction between the ionomer and the N-functional groups of the modified carbon supports, and analyze its influence on the MEA performance and particularly transport of both O_2 and protons inside the CL, as well as their correlation with the surface properties defined by ex-situ characterization techniques. Additionally, X-ray photoelectron spectroscopy (XPS) was applied to evaluate the interaction of the ionomer with the N-groups of the modified carbon support within the electrode as a function of the different type of functional groups.[25]

Experimental

Oxidation of carbon.—For each batch, 2 g of commercial carbon Ketjenblack EC-300J (AkzoNobel), denoted as KB, was mixed in a 250 ml flask with 100 ml 70% HNO_3 (VWR chemicals, Anala NORMAPUR). The suspension was immersed in a 70 °C pre-heated oil bath and continuously stirred under reflux for 2 h. After the heat treatment, the suspension was immediately filtered and rinsed with hot water multiple times, until the pH of the filtrate became neutral. The powder was dried in a vacuum oven at 80 °C for 17 h. The oxidized carbon is herein referred to as KBox.

N-functionalization of carbon via NH_3.—400 mg of the pre-oxidized carbon was placed in a tube furnace (CARBOLITE GERO GmbH & Co KG, Germany) for N modification. A direct inflow of the reacting gas via an internal tube minimizes its decomposition during operation. The procedure is as following: initially 15 min of flushing at room temperature with pure NH_3 (Air Liquide, ⩾99.98 Vol%); afterwards, a constant heating rate of 400 °C h^{-1} up to set temperature (T_{set}, °C) and hold for 2.5 h. The tube furnace was thereafter naturally cooled down to room temperature and purged with Ar flowing for 15 min to remove all NH_3 residues. The flow rate of 10 l h^{-1} was constantly kept for all gas species during these steps. The aforementioned nitrogen functionalization process was performed for three different T_{set}: 200 °C, 600 °C and 800 °C. The samples are labeled according to their respective set temperatures, e.g. N-KB 600 after being annealed at 600 °C.

Catalyst synthesis- Pt deposition.—Pt was deposited on all carbon supports (including the pristine KB as reference) by utilizing a polyol-method. 300 mg of the N-functionalized carbon was mixed with 200 ml ethylene glycol (99.8%, Simga Aldrich) and 100 ml deionized water in a 500 ml round bottom flask.[5] The mixture was bath-sonicated for 15 min to obtain a homogenous solution. Finally, H_2PtCl_6 solution (0.25 mol l^{-1}, obtained from solid $H_2PtCl_6{\cdot}6H_2O$, Alfa Aesar)-whose amount adjusted as per nominal loading required per carbon type- was added to the dispersion and stirred for overnight at 25 °C. The nominal Pt loading was set between 16.5 wt% Pt. The dispersion was immersed in a 120 °C pre-heated oil bath and stirred for 2 h under reflux to complete the Pt reduction. The obtained catalysts were filtered and rinsed with hot water (3 l per 200 mg sample) to remove all chloride residues. Afterwards, the samples were dried in a vacuum oven at 70 °C overnight. The final Pt loading was determined by ICP-OES and is shown in Table I for each type of catalyst.

Induced coupled plasma optical emission spectrometry.—The exact Pt content was determined conducting inductively coupled plasma (ICP) analysis using a VARIAN 715-ES system. Hereby, 7–11 mg of respective catalyst powder have been mixed with 2 ml H_2SO_4 (95%–98%, VWR chemicals, Anala NORMAPUR), 2 ml HNO_3 (69%, VWR chemicals, Anala NORMAPUR) and 6 ml HCl (37%, VWR chemicals, Anala NORMAPUR) in a microwave tube. The chemical digestion was conducted in a microwave (Microwave GO, ANTON PAAR) within 10 min it was constantly heated up to 120 °C and kept there for 10 min. From standard solutions of 1, 5 and 10 mg l^{-1} (H_2PtCl_6 in 2 mol l^{-1} HCl, 1000 mg l^{-1} Pt, MERCK KGAA), a calibration curve was constructed and the chosen wavelengths for the Pt determination were 203.646, 204.939, 212.863, 214.424, 217.468, 224.552 nm.

Elemental analysis.—A Thermo Flash 1112 Organic Elemental Analyzer (Thermo Finnigan) has been used for the elemental analysis of C, H, N and S (Table II). For this purpose, the samples were combusted in presence of V_2O_5 as oxidizer by dynamic flash at 1020 °C. The decomposition takes place in a manually stacked reactor of $WO_3/Cu/Al_2O_3$ layers. Gas chromatography (GC) determines and quantifies the resulting gases.

Microstructure analysis.—To investigate the micro and meso pore structure of the different carbon supports, N_2 physisorption isotherms were obtained at 77 K using Autosorb-1 (Quantachrome Instruments). The samples were put in a 4 mm diameter glass tube stacked with glass wool and a glass rod to minimize the dead volume. To reduce errors, the sample mass was controlled so that the absolute surface area exceeds 10 m^2 for each test. For at least 24 h, the samples were degassed under vacuum at 90 °C to remove any adsorbents as water and gas. Outgassing temperature was kept at this value to avoid decomposition of functional groups. The adsorption

Table I. Cathode specifications of 5 cm^2 MEAs: Pt catalyst loading on different carbon supports and the cathode Pt loading.

Catalyst type	Pt catalyst loading [wt%]	Cathode Pt loading [mg_{Pt} cm^{-2}]
Pt/KB	16.7	0.103 ± 0.003
Pt/N-KB 200	16.2	0.110 ± 0.002
Pt/N-KB 600	16.7	0.110 ± 0.001
Pt/N-KB 800	16.3	0.103 ± 0.005

Table II. Elemental bulk composition (CHN) of the different types of carbons. The oxygen content was estimated as the difference to 100% assuming only C, N, H and O atoms in the modified carbon support.

	Elemental analysis (wt%)			
Sample	C	N	H	O
KB	98.57	0	0	1.43
KBox	90.00	0.11	0.21	9.68
N-KB 200	93.48	0.84	0.12	5.56
N-KB 600	96.45	0.81	0.09	2.65
N-KB 800	94.41	1.91	0.20	3.48

and desorption isotherms were recorded in a range of $10^{-5} \leqslant p/p_0 \leqslant 0.995$ with p_0 referring to the saturation pressure and p the actual gas pressure. The most accurate technique to differentiate micro and mesopores is applying a density functional theory (DFT) model.[26] To evaluate the ratio of micropores (<2 nm) to mesopores (>2 nm), the DFT kernel QSDFT with a slit/cylindrical pores model was applied for the adsorption branch. This kernel considers a certain roughness and heterogeneity of the surface, preventing artificial gaps in the calculation.[11,27,28]

Water physisorption.—Water uptake measurements were recorded at 298 K in a Quantachrome Hydrosorb 1000 instrument. The samples were pre-evacuated for 72 h at 120 °C and 10^{-3} bar. Before starting the test, each sample was He-calibrated to define the exact sample weight. Water was used as an analysis gas from a manifold regulated to 100 °C. Each point was equilibrated within a pressure tolerance of 0.05 and equilibration time/equilibration timeout of 300/4000 s. The overall analytic time was 65 h for each sample.

Thermogravimetric analysis (TGA).—The thermal stability of the pristine, oxidized and N-modified carbon species was determined using thermogravimetric analysis. The measurements were performed in Ar with a TGA-DSC PERKINELMER STA-8000 and a heating rates of 5 C min^{-1} up to 1100 °C.

X-ray photoelectron spectroscopy.—XPS was carried out in ultrahigh vacuum (UHV) at room temperature using a monochromatized Al Kα X-ray source (1486.6 eV) excitation and a hemispherical analyzer (Phoibos 150, SPECS). All spectra were aligned to C 1 s graphitic peak (284.5 eV). For samples exhibiting charging, a flood gun (SPECS FG 15/40) was used to compensate surface charge. Theoretical cross-sections from Yeh et al. were used to calculate the elemental surface composition.[29] The N 1 s spectra were fitted using 8 components with individual binding energies indicated in parenthesis: pyridinic N (398.4 eV), hydrogenated pyridinic N (399.7 eV), pyrrolic N (399.9 eV), quaternary N (401.1 eV), protonated pyridinic N (401.7 eV), graphitic N (402.4 eV), hydrogenated graphitic N (403.8 eV) and N-oxide species (404.1 eV).[30–34] For details on these components, please refer to section "Molecular catalyst/ionomer interactions". Data processing was performed using the CASA XPS software. All components were fitted using Voigt type line shapes, Shirley background and FWHM of 1.5–1.6 eV.

To investigate the interaction between the ionomer and the carbon support, electrodes comprising various types of carbon supports and an I/C ratio of 0.25 were manufactured and subject to XPS analysis. The manufacturing procedure is similar to that described in the following MEA preparation section.

Transmission scanning electron microscopy (TSEM).—The morphology of the carbon-supported Pt catalysts was analyzed by using TSEM (Hitachi SU8030 SEM by use of a with a cold field emitter cathode operated at a 30 kV acceleration). The TSEM instrument was used in the TE mode (TEM image), in order to observe all of the Pt particles that are located on the interior and exterior surfaces of the carbon particles. On the same sample and the same location the SE mode (SEM image) was also used enabling the observation of the Pt particles located on the exterior surfaces of the carbon particles only.[3] By using this technique, we were able to evaluate the distribution of Pt particles on various carbon supports.

Membrane electrode assembly (MEA) preparation.—All membrane electrode assemblies (MEAs) were fabricated with the decal transfer method.[35] The catalyst powder was mixed with a low-EW ionomer dispersed in 40% H_2O/60% 1-propanol (3 M™ Dyneon™ PFSA (725 EW $\equiv g_{polymer}/mol_{H+}$)) and a specific water/1-propanol ratio (16–25 wt% H_2O in 1-propanol). The ionomer to carbon ratio (I/C) for the cathodic electrode was 0.65 in all cases. To obtain high decal quality and homogenous catalyst layer thickness during the coating, the ink recipe and viscosity (solid content of the ink) were optimized for each catalyst (see Table SI). All these ink components were merged in a 15 ml HDPE capped bottle containing 26 g of 5 mm ZrO_2 beads. The adding sequence was as followed: catalyst, water, 1-propanol, and finally the ionomer dispersion. The bottles were put onto a roller-mill (60 rpm) for 18 h at room temperature for homogenous mixing. Finally, the inks were coated onto virgin PTFE using a Mayer rod coater (ERICHSEN UNICOATER MODEL 490) with a coating speed of 10 mm s^{-1}.

For the anodes, commercially available 30 wt% Pt/graphitized-Ketjenblack (TEC10EA30E, TANAKA Kikinzoku Kogyo K. K.) was used for electrode manufacturing. The I/C was set to 0.65 and Pt loading 0.17 mgPt cm^{-2}, a value higher than the respective cathode loadings (see Table I), thus preventing any voltage differences that originate from the anodic electrode. A summary of the cathode specifications can be found in Table I. All electrode loadings (anode/cathode) were determined by weighting the decals before and after the catalyst layer transfer. The decal transferred membrane electrode assembly (MEA) was assembled by hot pressing a 10 μm membrane (GORE MX20.10) between the anode and cathode decals at 155 °C for 3 min with an applied force of 0.24 kN cm^{-2}. The hot press (LAUFFER PRESSEN, type: UVL 25.0) was preheated at 155 °C prior to inserting the assembly for decal transfer. In order to minimize edge effects and to control the active area, the MEA was sandwiched between two subgaskets (CMC Klebetechnik, type: PEM-Schutzfolie 61325). The measured thickness of the two combined subgaskets was around 88 μm. The size of the subgasket window defines as active area of the MEA (5 cm^2). For the MEA lamination in the subgasket, first a 10 min hot press procedure at a set temperature of 135 °C was conducted with an applied force of 0.135 kN cm^{-2} over the entire area. Thereafter, the hot press temperature was ramped down to 75 °C within 10 min without releasing the pressure. The lamination process was completed as soon as the temperature of 75 °C was reached.

Fuel cell assembly.—All the electrochemical testing for 5 cm^2 MEAs were conducted in a modified single-cell hardware from Tandem Technologies containing a 50 cm^2 active area graphite composite flow field (14 channel serpentine flow field[36] purchased from Nisshinbo). This setup employs a hardstop sealing concept, where the compression of the MEA is not defined on the clamping pressure of the testing hardware but rather controlled by the height of the uncompressible seal. The clamping pressure was set to 9 bar to seal the cell properly and avoid external leakage. The thickness of the incompressible fiberglass-reinforced PTFE-gaskets (Fiberflon) was chosen to obtain a 20% compression of the GDL. The GDL used in all experiments was 29BC with a nominal thickness of 235–240 μm (SGL Carbon). Figures S1 and S2 (available online at stacks.iop.org/JES/169/054520/mmedia) show a laminated framed MEA with an active area of 5 cm^2, including the sealing used during fuel cell operation, as well as the location of the MEA with respect to the flow field configuration.

Electrochemical Testing and Diagnostics

Fuel cell testing.—All fuel cell measurements were conducted on an automated a HORIBA FuelCon GmbH (Germany) single cell test station (typ 200 A FUELCON) equipped with a potentiostat (ZAHNER-Elektrik GmbH & CoKG) and additionally coupled with a booster. The latter ensures accuracy at low total currents, which is required because of the small active area. Pure hydrogen (99.999 % purity) and compressed air were used as anode and cathode reactant, respectively. For each type of MEA, two independent fuel cell measurements were performed and the average value with corresponding error bars to the standard deviation is depicted in all figures.

Activation procedure.—For all tests, the activation was identical via a voltage-controlled ramp-in procedure: a constant reactant flows of H_2/air were kept at 1.0/2.0 Nl min^{-1} and the cell temperature was set to 80 °C and 100% relative humidity (RH) on both anode and cathode sides with a backpressure of 170 $kPa_{abs,out}$. The voltage-controlled ramp is displayed as the followed sequence: 0.55 V for 45 min, 5 min at open-circuit voltage (OCV), and 10 min at 0.85 V. This protocol was repeated 10 times, resulting in a constant and stable performance.

Recovery step.—After the activation, each MEA undergoes a recovery step of 2 h holding at 0.1 V with a backpressure of 230 $kPa_{abs,out}$ at both sides anode and cathode, while the cell temperature was set at 50 °C and RH at 100%. The reactant flows of H_2/8.6% O_2 (by diluting air with N_2) were kept constant at 1.0/1.7 Nl min^{-1}, respectively. This recovery step eliminates any performance losses originated from reversible processes.[37]

Polarization curve.—All polarization curves for 5 cm^2 MEAs were recorded in galvanostatic mode using the EU harmonized protocol.[4,38] Two types of polarization curves were recorded. For the first one, herein defined as "wet operating conditions", the cell temperature was kept constant at 60 °C at 90% RH for both anode and cathode, while applying a backpressure (outlet controlled) of 170 $kPa_{abs,out}$ at both compartments. For the second polarization curve, herein defined as "dry operating conditions", the cell temperature was kept constant at 90 °C and 30% RH for both anode and cathode, while applying the same backpressure (outlet controlled) of 170 $kPa_{abs,out}$ at both compartments. In both cases, the reactant gas flows were kept constant with H_2/air at 1.0/2.0 Nl min^{-1}, respectively (counter-flow). This corresponds to a stoichiometry of 14.2 for H_2 and 12.1 for air at 2 A cm^{-12} (differential flows). The polarization curves were recorded starting from high current density with an interval of around 13 points until OCV. Each current density point was held for 10 min and the resulting voltage was averaged over the final 30 s (except at 0.05, 0.1 and 0.2 A cm^{-12} where only the final 30 s were recorded, see details in the EU harmonized protocol[4,38]). At specific current densities (0.1, 0.5, 1.0 and 2.0 A cm^{-2}), galvanostatic EIS spectra (using the Zahner potentiostat) were recorded with starting frequency of 20 kHz up to 10 mHz in order to determine and monitor high frequency resistance (HFR). Since the monopolar plates/flow field are made of graphite composite material with a relatively high resistance of 30.5 mΩ·cm^2, relatively high HFR values are to be expected. In order to determine the real MEA resistance, the resistance of the monopolar plates is subtracted from the measured HFR values. Analogously, the polarization curves are corrected for the monopolar plate resistances.

CO stripping.—CO stripping measurements were conducted to determine the ECSA of 5 cm^2 MEAs. Anodic and cathodic compartments were kept under ambient pressure during the entire measurement. Two measurements were conducted at a cell temperature of 80 °C, where the RH was set to 30% and 100% for each measurement (same value for anode and cathode). The anodic flow was kept constant at 0.5 Nl min^{-1} H_2, while the cathodic one was set to 3.0 Nl min^{-1} N_2 to purge the compartments until the cell OCV succeeds 0.15 V. CO adsorbing was achieved by flushing the cathode with diluted CO (0.2 Nl min^{-1} of 0.1% CO in N_2) for 30 min at 80 °C and 101 kPa_{abs} while holding the potential at 0.1 V. Thereafter, the cell was purged for 30 min using a N_2 flow rate of 0.5 Nl min^{-1} to remove all CO residues in the gas phase while keeping the cell voltage at 0.1 V. To remove the absorbed CO, cyclic voltammetry (CV) was performed between 0.053 and 1.0 V, with a scan rate of 50 mV s^{-1}. To verify the complete removal of CO in the gas stream and the electrode surface, two additional sweeps were recorded. The ECSA was determined by integrating the area of the first anodic scan with the subsequent sweep as baseline, using a specific charge of 420 $\mu C\ cm^{-2}_{Pt}$.

Limiting current measurement.—Limiting current measurements were performed to determine the total O_2 mass transport resistances. The measurements were conducted at 30% RH and 100% RH at 80 °C cell temperature. Flows were kept constant at 1 Nl min^{-1} H_2 and 2.04 Nl min^{-1} diluted air (2.4% O_2, 0.235 Nl min^{-1} air + 1.81 Nl min^{-1} N_2). In order to avoid surface recovery or change of the Pt/ionomer interface especially under prolonged dry operating conditions, the testing time was kept short (5 min holding time at 0.3 V and 2 min at 0.2 V). Similar testing procedure and protocol were used as described in Jomori et al.[39] and Du et al.[37] The measurements were conducted at 170, 230 and 300 kPa_{abs}.

Electrochemical impedance spectroscopy (EIS) in H_2/N_2 .—Protonic resistivity of the cathode CL was obtained by applying AC impedance spectroscopy under H_2/N_2 (1/2 Nl min^{-1}) at 0.5 V with peak-to-peak perturbation of 20 mV. The test protocol is similar as described by Liu et al.[40] Frequencies were varied with 20 points per decade between 100 kHz and 0.3 kHz (more precisely, 5 periods for frequency $<$ 66 Hz; 20 periods for frequency $>$ 66 Hz). To ensure reproducibility, three spectra were recorded. The spectra were acquired under two different operating conditions while keeping the cell temperature constant at 80 °C. RH was varied between 30% and 100% (same for both anode and cathode). In order to ensure accurate comparison between different RHs, the H_2 partial pressure was kept constant. A transmission line model was used to fit the EIS spectra to determine the proton resistivity. The specific proton resistivity (ρ, in Ω·cm) was calculated using eq. 2 from Du et al.[37]

Results and Discussion

Carbon and catalyst characterization.—Porous Ketjenblack carbon supports were N-functionalized using ammonolysis at three different temperatures (200 °C, 600 °C, 800 °C) and will be denoted as N-KB 200, N-KB 600[16] or N-KB 800, respectively. Some of physico-chemical analysis of the 200 °C, 600 °C N-modified catalysts was already reported elsewhere.[16] For the readers' convenience, we have included the aforementioned data for comparison reasons with the previously unreported N-KB 800.

Elemental analysis.—The total nitrogen contents determined by Elemental analysis (CHNO) is shown in Table II. All samples were synthesized aiming a nominal N loading of approximately 1 wt%. The unmodified carbon KB was used as a reference.

It is widely known that oxidation of carbon in concentrated HNO_3 leads to a surface functionalization with carboxylic, hydroxyl, and NO_x groups.[41] Unsurprisingly, some N-content was found to be present on the oxidized KB support, which was absent for the pristine KB (see Table II). The N-content further increases significantly during the heat treatment, as a result of the formation of pyrrol/pyridine/quartenary/pyridine-N-oxide/NO_x groups.[42,43] At the same time, the C-content increases (from 90.0 to 93.48–96.45 wt%) due to the loss of less stable O-containing functional groups during the heat treatment.

The carbon content determined by CHNO analysis (Table II) is in excellent agreement with that determined by XPS and by TGA analysis (see details in SI and Fig. S3).

X-ray photoelectron spectroscopy. X-ray photoelectron spectroscopy.—The presence and nature of the different N-containing functional groups on the different carbons support was examined by X-ray photoelectron spectroscopy (XPS). The N 1 s spectra of the carbon powders were fitted with 5 peak components: pyridinic-N, pyrrolic-N, quaternary-N, graphitic-N and NO_x species,[31,44–46] shown in Table III and Fig. S4. In the case of N-KB 200, a second type of NO_x species needed to be added for the fit (Fig. S4).[46] This group vanishes for all the other samples indicating its unstable chemical nature at temperatures above 200 °C.

The major fractions of N-functionalities are presented in pyridinic and pyrrolic groups, whereas graphitic groups display a minor contribution. A clear trend of the pyridinic and pyrrolic groups is discernable in correlation with the treatment temperature, where the former increases and the latter decreases in percentage with higher temperature (see Table III and Fig. S4).[31] While the NO_x-groups lessen with increasing heat treatment temperature, it seems that the fractions of quaternary groups reaches a maximum for heat treatment temperature of 600 °C. All above present the striking difference of the samples in chemical nature as a result of different surface modification and synthetic conditions. Furthermore, the near surface N at% content of N-KB 200, N-KB 600 or N-KB 800 was 0.8, 1.2, and 1.98, respectively, evidencing that the ammonolysis temperature >600 °C raised the N dopant amount significantly.

Porosity analysis.—N_2 adsorption isotherm analysis was utilized to investigate the effect of the synthetic route on the carbon microstructure, whose change could affect the performance of the catalyst in low Pt loaded electrodes.[10] Table SII summarizes the results from the BET and the QSDFT analysis (see Supplementary Information). As shown in Table SII, the overall surface area using DFT calculation (S_{micro}+S_{meso}) is not equal to the area obtained from BET calculation. This systematical overestimation of BET surface area is described in the literature as the contribution of micropore volume filling to the free surface coverage. An additional explanation is the fact that the density of nitrogen adsorbed in micropores is higher compared to liquid bulk nitrogen.[11] QSDFT determines the contribution of the micropores and mesopores to the total area (see experimental for more details). The area of the micropores (Fig. 1), for the N-KB 200 and N-KB 600, exhibited overall small changes compared to the pristine carbon. The latter is known to occur as a result of micropore blockage by functional groups.[5,47] The same was observed for the external area of the carbon support, where a slightly higher loss of mesopores was observed.[47] This was not observed for the sample that was heat treated at 800 °C. On the contrary, the N-KB 800 exhibits higher mesopores compared to the KB.

Hydrophilicity of N doped carbons.—In order to get insight into how different N-groups influence the physical properties of the support and how this in turn might affect the CL, water uptake measurements were conducted to investigate the wettability properties of the N-modified and pristine carbon supports (Fig. 2). The water uptake isotherms exhibited similar hysteresis shapes for all samples suggesting hydrophobic surfaces. Water uptake at 100% RH was essentially identical; small deviations between samples at RH close to 100% are most likely measurement artifacts, since the equilibration point can slightly vary at such high humidity. To draw conclusions about the hydrophilicity of N groups, the RH range of 40%–80% is relevant. The steeper the increase in water uptake is, the easier water molecules are being adsorbed by the surface of the sample and the more hydrophilic the sample appears. All N-modified carbons exhibited slightly higher hydrophilicity compared to the pristine KB: hydrophilicity trends are N-KB 200 > N-KB 600 > N-KB 800 > KB. Interestingly, in the H_2O desorption branch, all N-modified carbons exhibited similar hysteresis (30%–60% RH), suggesting a greater water retention ability compared to reference KB. The latter observations were also confirmed by normalizing the water adsorption isotherms to the BET area (Fig. S5), which ensures that the water uptake was not influenced by their respective difference in micro and mesoporous structure. In addition, to verify that the presence of Pt does not alter the hydrophobicity of the samples, we measured a Pt/KB catalyst under the same conditions as

Table III. Summary of XPS composition of the different types of carbons decomposed for five N-functionalities. Their content is given as fraction of one specific group over the entire amount of N, so it sums up at 100% overall different N-groups.

	Relative N group content (%)				
Samples	Pyridinic	Pyrrolic	Quaternary	Graphitic	–NO_x
N-KB 200	23.1	41.7	7.7	4.8	22.7
N-KB 600	40.2	26.5	13.6	4.5	15.2
N-KB 800	44.7	25.5	11.9	4.5	13.4

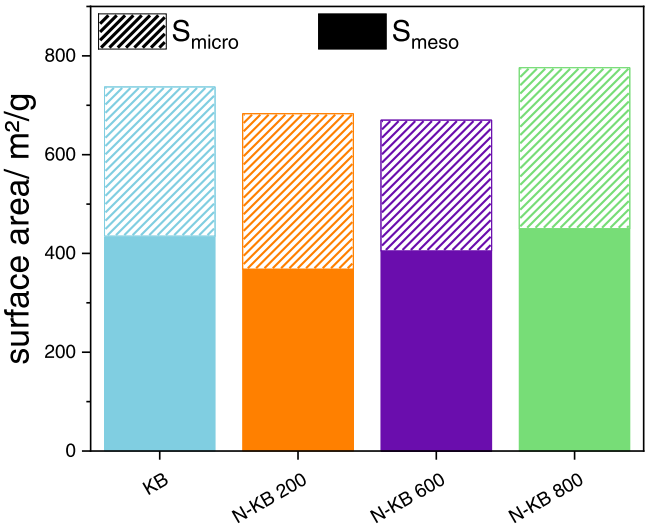

Figure 1. Pore analysis of the carbon structure: microporous surface area (S_{micro}), mesoporous surface area (S_{meso}) and sum of micro- and mesoporous surface area (S_{meso}+S_{micro}), as calculated using QSDFT, and their corresponding ratio (S_{meso}/S_{micro}) for each type of carbon used in the present study.

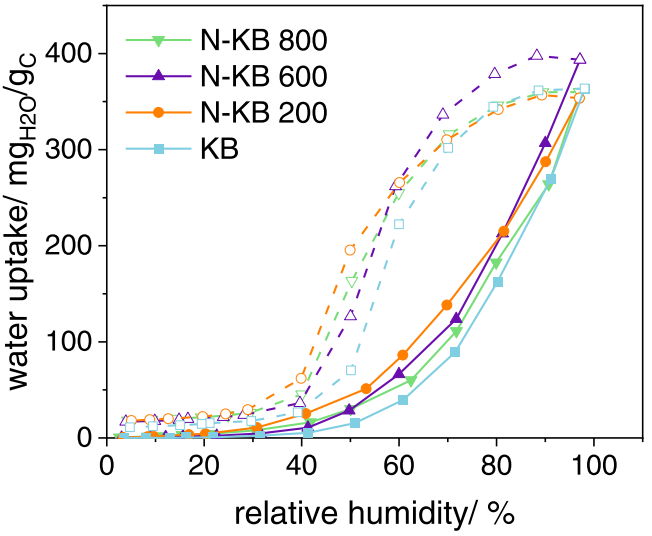

Figure 2. Water uptake determination of the different carbon supports by water adsorption isotherm (mg_{H2O}/g_C) as a function of relative humidity at 298 K. Solid lines illustrate the adsorption curve, whereas dashed lines the desorption curve.

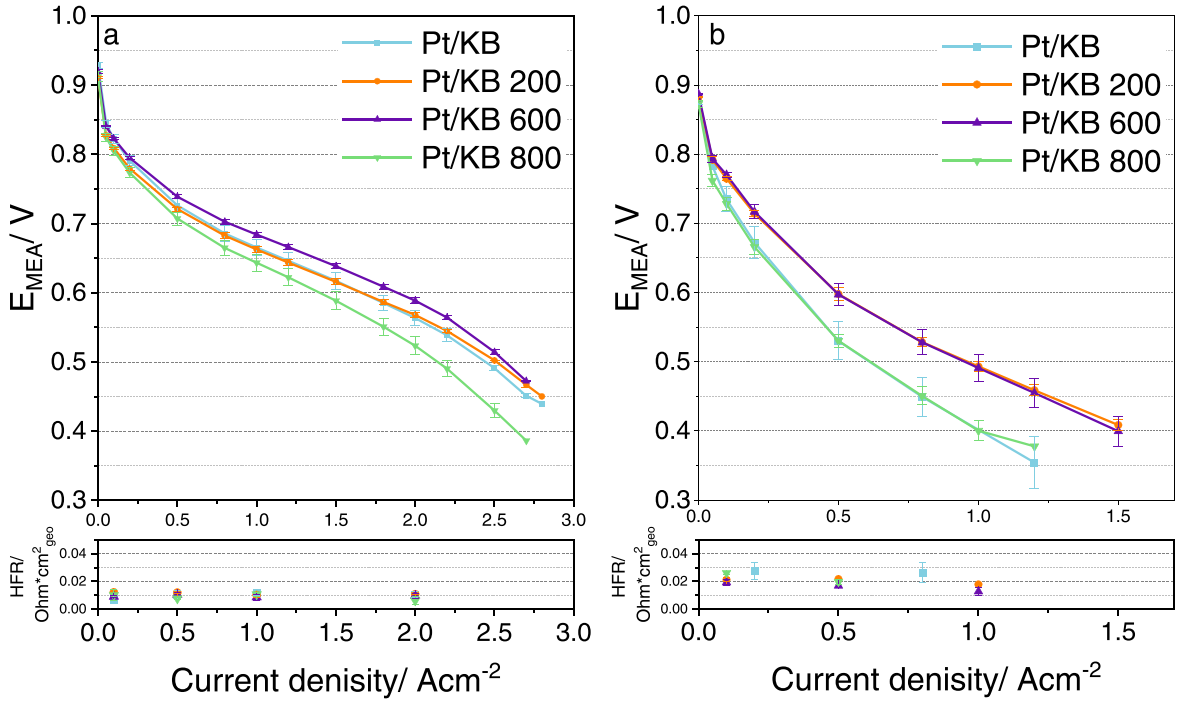

Figure 3. Effect of the cathode catalyst type on the 5 cm^2 MEA performance under various operating conditions. The average Pt loading of the cathodic electrodes was 0.107 ± 0.005 mg_{Pt} cm^{-2}. a. The cell temperature was kept constant at 60 °C, 90% RH and a backpressure of 170 $kPa_{abs,out}$ were applied for both anode and cathode compartments and b. the cell temperature was kept constant at 90 °C, 30% RH and a backpressure of 170 $kPa_{abs,out}$ were applied for both anode and cathode compartments. Both types of polarization curves were measured under constant differential flow (H_2: 1 Nl min^{-1} and air: 2 Nl min^{-1}). The voltage was corrected for the monopolar plate resistance (0.0345 Ω·cm^2). On the bottom of each graph, the corresponding HFR values corrected for the monopolar plate resistance are depicted. With this correction the HFR from the MEA would be three times higher under dry conditions compared to wet ones. Error bars represent the mean absolute deviation from two independent measurements.

its support KB. It was clear that the hydrophobicity was not significantly affected by Pt deposition as shown in Fig. S6. However, a blocking effect of the Pt particle can be observed, indicated by a significant reduction of the overall water uptake.

Catalyst characterization.—Subsequently, the supports were platinized following a previously established protocol.[16] The three resulting N-modified carbon-supported Pt nanoparticle catalysts for oxygen reduction will henceforth be denoted as Pt/N-KB 200, Pt/N-KB 600 and Pt/N-KB 800. Catalyst with unmodified Ketjenblack (Pt/KB) was used as a reference. The Pt loading on the different carbon support was evaluated via ICP-OES and results are shown in Table I. The average Pt particle size from TSEM was found to be 2.5 nm (refer to Tables SIII in the SI). As depicted in Fig. S9, the Pt-particles are mostly deposited at the exterior surface of the carbon support. It is evident from the TSEM micrographs, that the Pt distribution and localization does not change with N-modification of the carbon support. Those findings are also pointed out in our previous publication Ott et al.[16]

Electrochemical Characterization

Effect of N-functionalization on PEMFC performance.— Single PEMFC experiments were conducted on 5 cm^2 membrane electrode assemblies (MEAs) under different operating conditions. Figure 3 shows the effect of the carbon supports on the MEA performance under two extreme relative humidity values, in particular in Fig. 3a at 60 °C and 90% RH, herein defined as "wet operating conditions"; and in Fig. 3b at 90 °C and 30% RH, herein defined as "dry operating conditions". These two operating conditions were chosen to translate our findings to big active area MEAs as used for automotive applications. The "dry conditions" mimic the gas inlet at a high-power mode, whereas the "wet conditions" present those at the outlet region of an automotive cell at low power

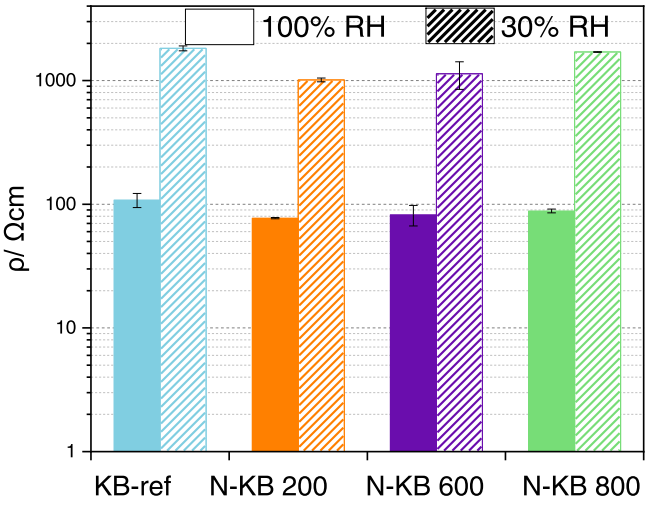

Figure 4. Effect of relative humidity on the proton resistivity of the cathode CL comprising different types of catalyst. The proton resistivity was determined from impedance spectroscopy in H_2/N_2 via fitting with a transmission line model. Conditions for the impedance are: cell temperature of 80 °C, as well as 100% RH (solid bar) or 30% RH (dashed bar). Error bars represent the mean absolute deviation from two independent measurements.

mode, where the ORR produced water is accumulated in the gas stream. All polarization curves were recorded under constant differential flow of 1 Nl m^{-1} of H_2 and 2 Nl m^{-1} of air, while keeping both anode and cathode backpressures at 170 $kPa_{abs,out}$.

In the case of "wet operating conditions" (Fig. 3a), it is evident that the MEA prepared using the Pt/N-KB 600 catalyst exhibited the highest performance and power density.[16] While Pt/KB and Pt/N-KB 200 exhibited very similar performance, a further increase of

ammonolysis temperature to 800 °C (Pt/N-KB 800) resulted in a fairly poor polarization behavior, ranging even lower than the reference Pt/KB. In addition, MEA with Pt/N-KB 800 showed signs of electrode flooding even at low current densities. We hypothesize that the increasing mass transport losses in Fig. 3a are largely related to an increasingly inhomogenous ionomer distribution which, in combination with the strong ionomer swelling under the wet operating conditions (60 °C and 90% RH), should lead to hindered gas transport within the electrode.[11]

Figure 3b depicts the performances under "dry operating conditions", where it is expected that an inhomogenous ionomer distribution would result in a particularly poor proton conductive pathway within the CL and thus in a poorly performing MEA.[11]

Proton resistivity in catalyst layers.—As mentioned previously, a sufficient supply of protons and reactant gas on the Pt surface is critical for a good MEA performance under high current densities. The quality of the protonic conductive pathway within the CL is macroscopically represented by the specific proton resistivity ρ_{H+},[11] which was evaluated at different RHs as illustrated in Fig. 4. In order to demonstrate the accuracy of our fitting for the ρ-determination, Figure S8a/b additionally show representative H_2/N_2 EIS spectra and their corresponding fitting under both 30% and 100% RH. At 100% RH, the CLs comprising Pt/N-KB 200 and Pt/N-KB 600 appeared to have exhibited slightly lower ρ_{H+} compared to the other two type of CLs (Pt/KB and Pt/N-KB 800). However, under such wet conditions, differences in ρ_{H+} between different CLs have to be treated with caution. It is known that the error during the determination of the resistivity is relatively large, due to the difficulty of fitting a transmission line model when the proton conduction resistance is very low.[40] At 100% RH, liquid water is of excess within the CL and thereby compensates for any inhomogeneity in the ionomer distribution. Consequently, taking this and the slight differences of the proton resistivity across all the tested CLs into consideration, we conclude that the observed performance difference depicted in Fig. 3a cannot be rationalized on the basis of proton transport resistivity only.

As expected, the ρ_{H+} values at 30% RH are considerably higher than those detected under wet conditions, reducing the relative error of their evaluation. Here, the value of Pt/KB is in good agreement with the values observed in literature for high surface area carbons using low equivalent weight ionomers with similar I/C.[9] Figure 4 clearly evidences that the MEAs comprising Pt/N-KB 200 and Pt/N-KB 600 supports exhibited lower ρ_{H+} values compared to reference KB (agreeing well with Ref. 37). Surprisingly, the Pt/N-KB 800 exhibited no better proton conductivity than the reference KB. Therefore, it is evident that not all types of surface N-functionalization of the carbon support automatically results in an enhancement of proton transport.

A plausible explanation for the observed differences in the proton resistivity at 30% RH could be attributed to the different water retention properties, which might in turn affect the amount of water that is "trapped" at the Pt/ionomer interface when the overall RH is lowered in the CL bulk. This hypothesis is supported by the observation that N-KB-200 and N-KB 600 exhibited higher water retention compared KB (based on water adsorption isotherm in Fig. 2). Nonetheless, it appears that the better water retention ability of N-KB 800 (similar to those of other NH_3-treated carbon) compared to the KB, is not reflected in the proton resistivity. The latter might be a further indication of poor ionomer distribution for the case of N-KB 800.

In order to further support our hypothesis, describing an effect of the ionomer distribution on the blockage of the porous structure, corresponding electrode layers were investigated via N_2 adsorption isotherms.[11,24] Figur S7 shows the pore area distribution curve plotted as d*S*/d(*d*), where the area under the curve is also directly proportional to the surface area.[11] It is clear that N-KB 800/ionomer and pristine KB/ionomer possess the highest ratio of micropores to mesopores within the CL. It is known that the pore size region of 3.5–12 nm is strongly linked to blocking effect by the ionomer, where a more homogenous ionomer distribution would result in a stronger reduction of the pore surface area in this specific region.(see Fig. S7 comparison with N-KB 200/ionomer or N-KB 600/ionomer).[11] It can therefore be concluded from Fig. S7b that the quality of ionomer distribution decreases in the following sequence of ammonia-modified carbon supports: N-KB 600 > N-KB 200 ≈ KB > N-KB 800.

This supports our hypothesis that a moderate surface N-functionalization (heat treatment in NH_3 at 200 °C or 600 °C) of the carbon support enhances charge transport by a more uniform ionomer distribution.[5,9] Overall, our analysis of the ρ-values tested at 30% (Fig. 4) RH is in good agreement with the findings of pore blockage in Fig. S7 and the performance trends in Fig. 3, accounting for a significant portion of the observed differences. However, it is apparent that other influential factors exist besides the proton conductive pathway, a point which will be investigated further on.

Oxygen transport resistance.—We now turn to the role of oxygen mass transport losses to explain the observed performance trends of Fig. 3. The detailed oxygen mass transport resistances were evaluated via limiting current method (see supplementary information for details). Measurements were conducted at both 30 % and

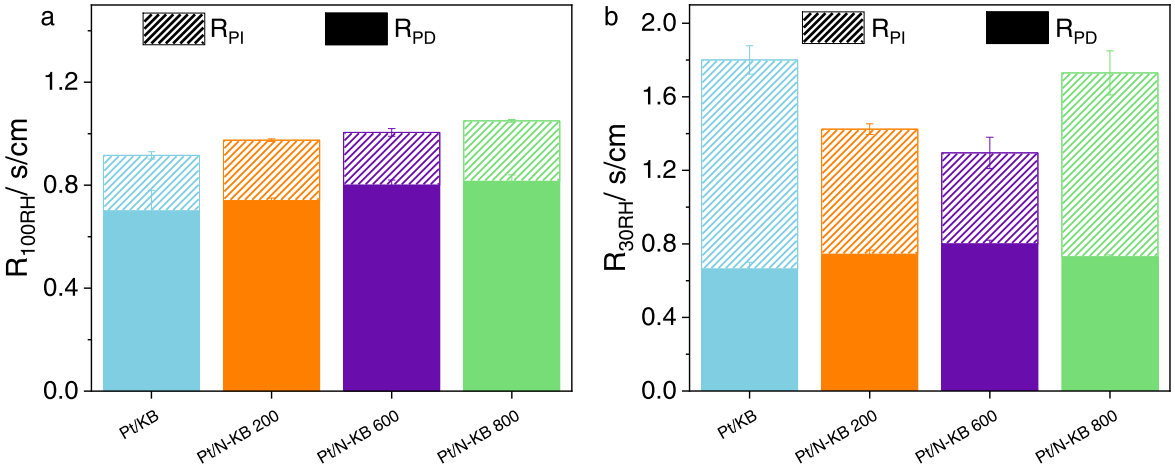

Figure 5. Comparison of total O_2 mass transport resistance (sum of solid and hatched bars) determined from limiting current measurement, which can be separated into a pressure dependent term (R_{PD}) and a pressure independent term (R_{PI}). (a) at 80 °C, 100% RH and (b) at 80 °C and 30% RH. The error bars correspond to the standard deviation between independent measurements with two different MEAs for each type of catalyst layer. Absolute pressures were set at 170 kPa_{abs} on both anode and cathode sides.

100 % RH, with the resulting mass transport resistances deconvoluted into pressure dependent $R_{PD,}$ and pressure independent terms R_{PI} (Fig. 5).[48]

It may be observed from Fig. 5 that the pressure dependent terms (R_{PD}) have slight variation among all cases ($0.74 \pm 0.06\ s\ cm^{-1}$). This discrepancy is not expected as it is known that R_{PD} is almost entirely determined by the GDL properties which are expected to be constant over all tests of various carbon supports. It shall be emphasized that the compression of the GDL was kept the same throughout the measurements ($20 \pm 1\%$), thus it could not have made the difference. One possible explanation could be attributed to the different batches of the GDL used in this study, which might possess slight variations in the GDL microstructure and hydrophobicity.

All four CLs exhibited similar R_{PI} values at 100 % RH. This is in good agreement with the work published by Harzer et al.,[9] where N functionalization of a KB carbon support with an I/C = 0.65 (like in our case) did not result in significant benefits with respect to oxygen transport resistances. This is primarily due to the very low effective ionomer film thickness over the high surface area carbon support, where it is known that a significant fraction of the ionomer is being absorbed into the carbon nanopores.[40] Therefore, it is evident that the mass transport resistances measured at 100 % RH do not contribute to any additional voltage losses observed in the "wet" polarization curves (Fig. 3a), whereas those losses rather might originate from local flooding within the CLs. Latter is caused by high water production rates during the acquisition of the polarization curves at high current densities (note that flooding does not occur during the limiting current measurement due to little water production under diluted O_2 conditions).

By lowering the relative humidity to 30%, the effects of varying ionomer distributions on the mass transport resistance become more pronounced. The mass transport resistances at 30% RH are significantly higher compared to the ones at 100 % RH, in accordance with literature.[49,50] Comparing the trends of various carbon support with their respective polarization performances, it becomes clear that the two catalysts with better performances under dry operating conditions (Fig. 3b), Pt/N-KB 200 and Pt/N-KB 600, exhibited also significantly lower R_{PI} at 30% RH. As reported in literature, R_{PI} mainly comprises the oxygen transport resistances arising from Knudsen diffusion[16] as well as the diffusion resistance through the ionomer towards the catalyst active sites. Since Pt deposition on all types of carbons (with and without N-modification) was done using the same polyol method (see experimental section), it was expected that all catalysts had similar percentage of external vs internal Pt particles with respect to the carbon surface.[16] This was confirmed by TSEM images in the present study, given in Fig. S9 for all tested catalysts. Thus, we can exclude any effect of the Pt-distribution and Pt-location onto the MEA performance. This implies that the Pt location is not expected to exhibit any significant influence on the observed trends in R_{PI}.[3,9,10] Hence, the difference in R_{PI} observed at 30% RH can solely be attributed to the difference in the Pt/ionomer interface (ionomer film thickness and distribution) or the carbon porous structure.[7] The data further evidences that the CL with N-KB 600 showed even lower R_{PI} values compared to the one with N-KB 200. This agrees well with the observed higher ECSA values (see Fig. 6, spider diagram), presenting a larger number of active sites per unit active area for O_2 adsorption and ORR. We note that NH_3-etching during ammonolysis may roughen the catalyst support surface and generate pores with more favorable sizes that are accessible to Pt particles, which was part of our original hypothesis in a previous study.[16] However, new evidences regarding the unexpected higher mass transport resistance of N-KB 800 makes the hypothesis of contributions of etching of the pores rather unlikely, despite the latter having a higher amount of mesopores compared to the N-KB 200 and N-KB 600 (Fig. 1).

From our proton and oxygen transport analyses above in combination with the MEA performance, we conclude that the presence of functional N groups on the carbon support surface alone does not guarantee homogenous ionomer distribution and hence high MEA performance. The poor performance of the N-KB 800 under wet and dry conditions suggests that other physico-chemical properties must have influenced the ionomer distribution during the electrode manufacturing process. These may include the capacitive characteristics of the electrochemical double layer as well as the nature of the functional N-groups on the surface of the support and their ionomer interactions. It appears that not the presence of N-groups alone determines the resulting ionomer distribution and the fine details of the CL morphology. Other changes such as oxygen content, wettability and porosity induced during the modification process might facilitate a better ionomer distribution by altered catalyst/ionomer interaction origin from acid-base interaction or van der Waals forces.

Correlation of ECSA and ionomer coverage with other electrochemical characteristics.—In order to gain a deeper insight in the ionomer distribution within the cathode CL, we conducted further electrochemical measurements to evaluate the ECSA and the double layer capacitance (C_{DL}) at various RHs. While the ECSA only contains information about the active surface area of Pt sites, the double layer capacitance is generated by the entire electrochemically accessible interfacial area between solid and ionomer/liquid, including that of the carbon support. Figure 6 depicts a spider diagram showing the correlation of all electrochemical characterization described in the previous sections to the ECSA at both wet (blue) and dry (orange) operating conditions. Based on the structure of the spider diagrams, it can be suggested that the catalyst that performs the best in both wet and dry conditions (i.e. covers the larger area in the diagram) is the one that exhibits the most favorable electrochemical properties.

Under dry conditions, the influence of the homogeneity of the proton conductive pathway on the performance can also be directly reflected by the normalized ECSA values, Fig. 6. By comparing the ECSAs at dry conditions, we demonstrate that the ECSAs of Pt/KB and Pt/N-KB 800 are significantly lower compared to the ones of Pt/N-KB 200 and Pt/N-KB 600. Under dry operating conditions, it is known that the MEA performance strongly correlates with the Pt availability and the proton accessibility within the cathode CL.[16] Therefore, we may deduce that the Pt utilization (dry proton accessibility) is the highest for Pt/N-KB 600. It can be observed from Fig. 6 that the MEA performance under dry conditions is well correlated with the ECSA at same operating conditions (note the connection lines between these two characteristics are relatively parallel to the "spider web").

Under wet operating conditions, no clear correlation can be observed between the ECSA and cell performance (note in Fig. 6 that some of the connection lines between these two characteristics are highly non-parallel to the "spider web"). Thus, the performance differences of the N-modified catalysts do not lie in the fraction of free Pt sites but need to be investigated further. Even though Pt/N-KB 800 provides a decent Pt availability, the MEA reveals drastic voltage losses under wet operating conditions. Such indicated flooding effects at high current densities origin from the physico-chemical properties of the cathode CL itself. In addition, the resistance on the Pt/ionomer interface is reverse proportional to the ECSA under the same Pt loading.[8] By comparing the trend in Fig. 6, this is in very good agreement with our findings for all catalysts.

Based on the summary electrochemical properties of each catalyst layer depicted in the spider diagrams (Fig. 6), it is clear that the poor performance of the N-KB 800 under both wet and dry conditions suggests that other physico-chemical properties must have influenced the ionomer distribution during the electrode manufacturing process. These may include wettability, pore structure, van da Waals forces, the capacitive characteristics of the electrochemical double layer as well as the nature of the functional groups on the surface of the support and their ionomer interactions. It also gets clear that the resulting MEA performance originates from a very complex interplay between different electrochemical

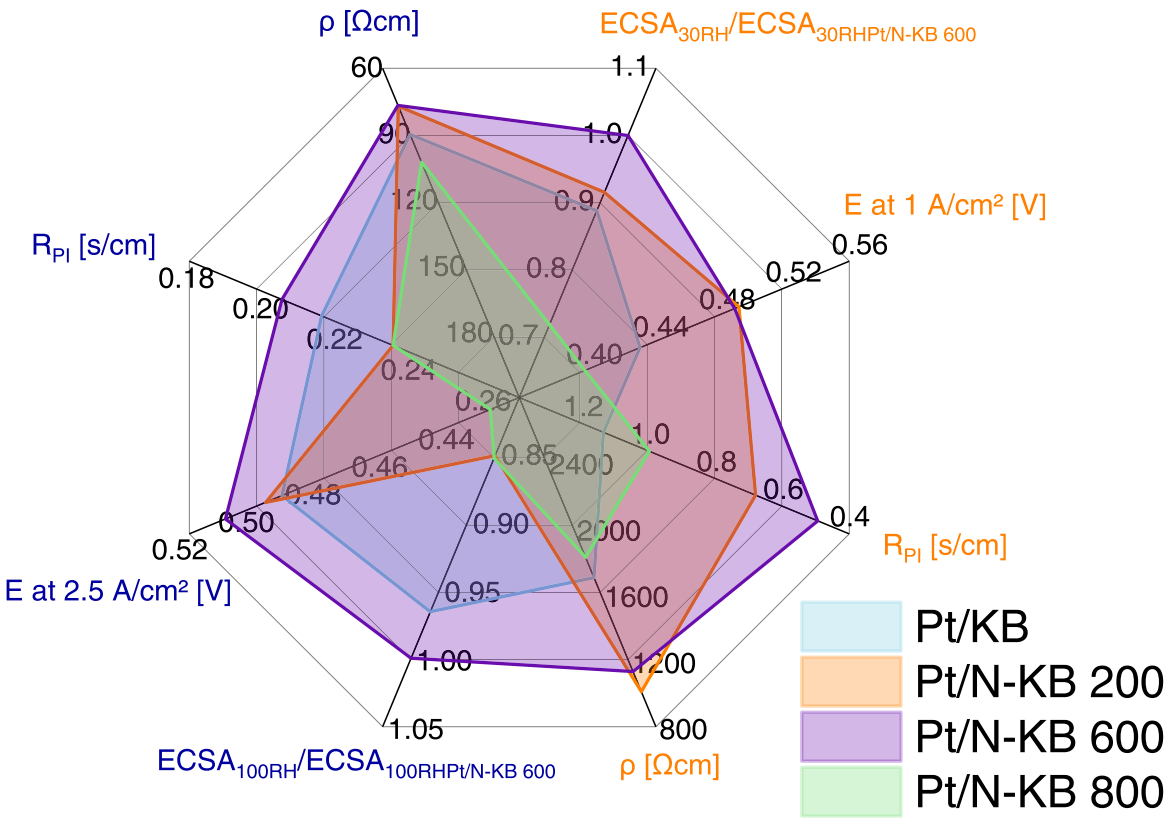

Figure 6. Spider diagram depicting the correlations of all electrochemical characterizations: ECSA, pressure independent mass transport resistance (R_{PI}), proton resistivity (ρ) and cell voltage (E) at high current density. Orange values represent the data obtained at 30% RH, while the blue colored values at 100% RH. All parameters are given as absolute values except ECSA. For comparison reasons, the ECSA values are normalized to the corresponding value of Pt/N-KB 600 at 30% and 100% RH, respectively.

parameter (ECSA, oxygen mass transport resistance, proton pathways) and physico-chemical properties of the catalyst/catalyst layer (ionomer distribution, porosity, wettability, Pt-location, catalytic kinetics). Thus there is not one pre-dominating factor but rather the sum and interplay of all different parameters have to match and be enhanced for optimized performance.

The double layer capacitance C_{DL} as a function of RH may provide additional information regarding the ionomer distribution across the entire electrochemical interface (Fig. 7). To understand the measured C_{DL} data of the electrodes with N-modified carbon supports, it is important to recall how such a defect in the carbon matrix may affect its capacitance. Different fundamental aspects need to be considered to explanation the overall C_{DL} increase with introduction of N-groups. First, C_{DL} is affected by the quantum capacitance. This quantum capacitance is determined by the density of states (DOS) at the Fermi level, on which the N-defects within the C matrix exert a direct influence. For instance, pyrrolic N donates electron density to carbon p_z orbitals, whereas pyridinic N acts as a p-dopant, withdrawing electron density from the carbon matrix.[51] On the other hand, experimental C_{DL} has pseudo-capacitance contributions originating from reversible faradaic charge transfer at O and N sites.[52,53] Hereby, pyridinic and pyrrolic groups play a rather major role in increasing C_{DL} what is in correlation with the trend in Fig. 7.[54–56] Additionally, hydrophilic polar sites enhance the wettability and result in increased accessible electrode surface due to ionomer and water penetration.[57,58] Here, we denote the ratio $\theta = C_{DL}(30\%\ RH)/C_{DL}(100\%\ RH)$ as an descriptor for the effective "ionomer coverage". θ helps in identifying differences, among N-modified carbons, in the coverage of the ionomer over the entire catalyst. As one can clearly see from Fig. 7a, C_{DL} increases from dry to wet operating state and with N-modification. Under humidified conditions, water enables an electrochemical accessibility for ionomer-uncovered regions. Especially under wet conditions, the extend of the C_{DL} for N-modified catalysts correlates with the MEA performance resulting in the best performing catalyst as Pt/N-KB 600. The data of Fig. 7b suggests that the ionomer coverage of the Pt/N-KB 600 is the highest, supporting or claims of beneficial catalyst layer configuration with ionomer distribution towards MEA performance. The extend of ionomer coverage (θ) seem to depend on the C_{DL} under dry conditions. This can be explained by the fact that the carbon/Pt ↔ ionomer interface determines the C_{DL} value alone, under dry operating conditions, thus the broader this interface becomes with increased ionomer distribution, the higher the C_{DL} values get.

Molecular catalyst/ionomer interactions.—In order to understand the molecular interaction between functional surface N groups and the ionomer, comparative XPS measurements were conducted. First, high resolution XPS spectra of the N 1s core level range of differently N-modified carbon support were collected in absence of ionomer (discussed in detail in previous section). Individual samples were compared to a set of analogous spectra collected from thin carbon layers comprising the carbon supports mixed with ionomer at an I/C ratio of 0.25. Considering the inelastic mean free path of the electron after initial X-ray excitation of the XPS beam, this reduced I/C ratio (compared to the one used for MEA manufacturing and in situ testing) was chosen to enable a sufficient surface sensitivity of XPS even if the carbon surface is covered underneath a thin layer of ionomer.

As already mentioned in previous XPS section, the N 1 s spectra of the carbon powders in absence of ionomer were fitted with 5 peak components: pyridinic-N, pyrrolic-N, quaternary-N, graphitic-N and NO_x species,[31,44–46] shown in Table III. In case of the so called pyrrolic group different N-functionalities as amine, imide, amide,

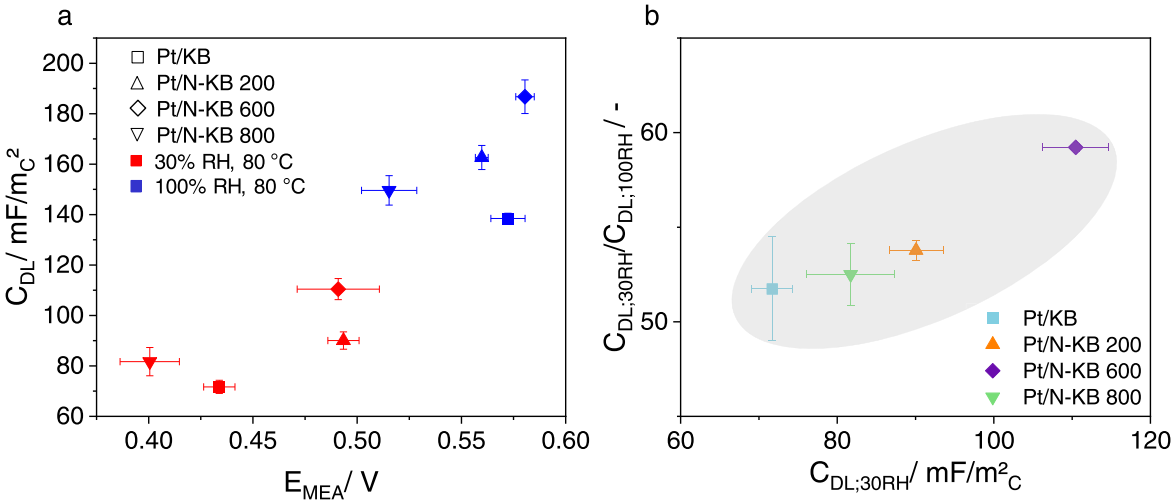

Figure 7. (a) Double layer capacitance (C_{DL}) of Pt/N-Ketjenblack test series under dry (red) and wet (blue) conditions correlated to the MEA current density at 1 and 2 A cm^{-12}, respectivitly. Calculated from 5 cm^2 MEA at T_{cell} = 80 °C, constant anodic flow of 0.5 Nl H_2 and cathodic flow of 0.5 Nl N_2 during cycling voltammetry. Relative humidity was set as 30% RH and 100% RH for dry and wet conditioning, respectively. C_{DL} was acquired from cyclic voltammograms (with a scan rate of 50 mV s^{-1} and a voltage range of 0.053 V–1.2 V) at a voltage value of 0.45 V and normalized to the corresponding BET surface area of the pure carbon. (b) Displays the ionomer coverage descriptor θ ($C_{DL30RH}/C_{DL100RH}$) in dependence on the C_{DL} under dry conditions.

lactam and pyrrol overlap in the same region and will be summarized in one group. However, for the case of N-modified carbon supports coated with ionomer, the previously applied fitting pattern of 5 peaks does not sufficiently represent the experimental data. Therefore, the deconvolution set had to be extended by three additional peaks denoting the protonated N-species with ionomer interaction as given in Fig. 8a.[30–32,34,44–46,59,60]

The most striking difference between the XPS spectra is a significant shift of peak intensity toward higher binding energies (BE) in the presence of ionomer (Fig. 8c). Since all spectra were aligned to their corresponding C 1s sp^2 peak (Fig. S10), charging effects can be excluded. Therefore, the origin of the BE shift is a chemical interaction of the surface N groups with atomic centers of the ionomer. Considering the basic/nucleophilic nature of the surface N groups and the acidic character of the sulfonate sidechain groups, a Brønsted acid-base interaction can be expected, where basic N-species included in the group of pyridinic-N and graphitic-N will get protonated by the sulfonic ionomer groups. This would cause a depletion in local electronic density near the N centers and slow down the escaping photoelectron, thus explaining the upward shift in BE.

For protonated N-species, Artyushkova et al. specified the typical range from 401.5 to 403.5 eV.[30] It shall be noted that the main contribution of the protonated N-species can be protonated pyridinic and graphitic groups, whereas some of the pyrrolic N groups (such as amide, imide, pyrrol, lactam) are neighbored to electron withdrawing oxygen groups or provide no free electron pair consequently expected to only form highly unstable protonated species so their contribution is omitted.[30,61] Indeed, Fig. 8c depicts that the presence of the ionomer results in a BE shift of +1.5 eV from graphitic-N to protonated graphitic-N, as well as a shift of +1.3 eV and +3.3 eV from pyridinic-N.[32,34] We need to mention that the protonation of a pyridinic N seems to have created two XPS peaks: the peak at 401.7 eV is expected to describe protonated pyridinic species (referred to as protonated pyridinic N), whereas the other at 399.7 eV (referred to as protonated/hydrogenated N) overlaps with the peaks expected for hydrogenated N-species such as lactam, imine, etc. Those groups could already be present in the pure N-modified powder, but can only be decomposed from the pyrrolic peak after interaction with ionomer as a result of partial protonation of some specific groups. The term "hydrogenated" is used to be in line with the literature.[30,32,34,62] It shall be mentioned at this point that hydrogenation, by means of an redox reaction where H_2 molecules are added to existing N-C bonds, can be excluded due to the mild reaction conditions during adding of ionomer (no catalyst, nor high temperature nor high pressure). Therefore, we want to specifically point out that those groups do not describe an N-group after hydrogenation but rather the protonated species of the second XPS peak describing a protonated pyridinic-N and remaining hydrogenated-N groups as lactam, imine, etc. but excluding any N-species of the pyrrolic group.[30]

A further deconvolution of the protonated/hydrogenated N species into charged and uncharged ones is not possible. Density functional theory (DFT) studies claimed strong coulombic interaction between charged groups, as included in those three additional peaks after ionomer coating, which in turn could result in a more homogenous ionomer coverage.[25,63,64]

As the fractions of N content differ slightly for each carbon support (see Table II), the total amount of hydrogenated/protonated species within the ionomer coated layer does as well. Figure 8d shows a correlation between the increased performance at high current density with the increasing total protonated species in the CL. It needs to be mentioned that the fraction of uncharged species in the hydrogenated/protonated N cannot be subtracted or determined/decomposed at this point. The performance under wet operating conditions strongly depends on the catalyst layer pore structure defined by the ionomer coverage, where ill-distributed ionomer would block the CL, resulting in flooding effects at high relative RH (Fig. S7). Hence, the higher amounts of positively charged N-groups are directly correlated to a stronger ionomer interaction and goes alongside with increased MEA performance. A clear linear correlation is discernible with increased fractions of positively charged N-groups which strongly interact with the negative sidechains of the ionomer during the electrode preparation. This emphasizes the N-functional groups, their chemical nature and interaction with the ionomer as one parameter facilitating a more homogeneously distributed ionomer layer. Nevertheless we want to mention that this is only one part of a much more complex interplay within the catalyst layer but seems to be a very important one.

The overall distribution and homogeneity of the ionomer is most likely also affected by other parameters such as the oxygen groups and surface chemistry including water uptake and surface area/porosity altering van da Waals forces between the ionomer and the catalyst. There seems to be an inverse correlation between the MEA performance and oxygen content (see Table II). However, the expected groups on the carbon surface such as carboxylic or

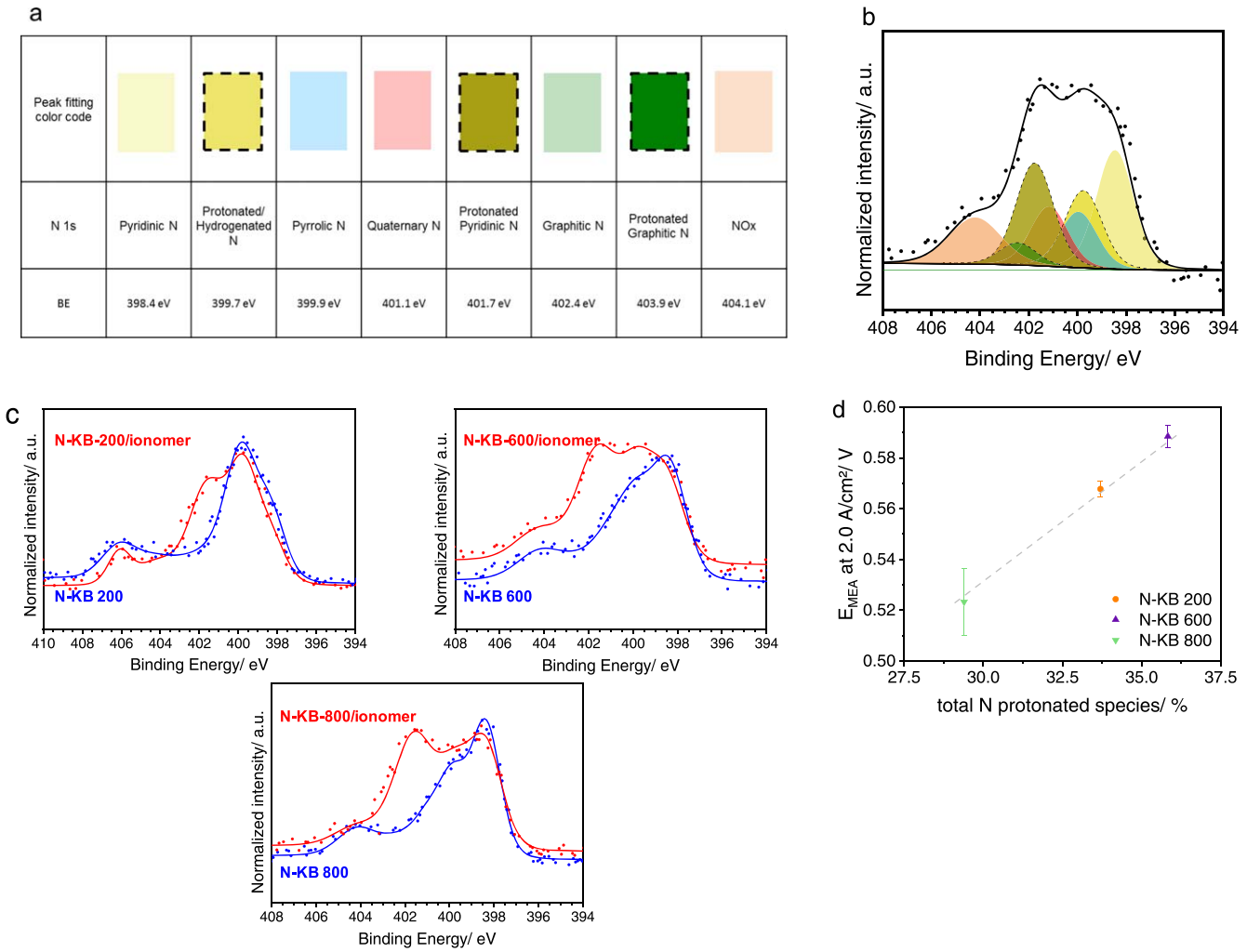

Figure 8. XPS spectra and analysis of the different carbon supports. (a) table for XPS deconvolution according to the specific N-groups including protonated/ hydrogenated groups after ionomer coating. (b) spectrum of N-KB 600/ionomer including peak deconvolution for individual N-functionalized groups. (c) Comparison of N 1s XPS fittings of the different N modified carbon support materials as synthesized (blue lines) and after being coated with a thin ionomer layer (red line). (d) Correlation of the total N protonated species (sum of "protonated" and "hydrogenated" N-groups) in the C/ionomer coating with the performance of the corresponding Pt/C electrode at high current density at 90% RH and 60 °C at 2 A cm^{-12}.

hydroxyl groups are very unlikely to get protonated by the ionomer. In addition, for a similar analysis as we conducted for the N-groups it is very difficult to deconvolute the O 1s spectra (Fig. S11) since the number of contributions from different oxygen functionality in this region is very large. In literature, researchers avoid to deconvolute the O 1s spectra since the resulting fitting can vary drastically depending on which groups are fitted.

With this investigation of the ammonia based N-modification and the effect of N-groups we want to add a piece to the puzzle for an overall view of the very complex catalyst layer and its configuration during operation. This work tries to empathize researchers not to focus only on the intrinsic catalytic activity changes with support modification and stability of deposited Pt nanoparticles but also on the support/ionomer interaction and its resulting morphology.

Conclusions

This experimental study gives an insight into the carbon support modification concept while trying to shed light on the origin of the enhanced MEA performance. At two very extreme MEA operating conditions, either wet (at 60 °C, 90% RH) or dry (at 90 °C, 30% RH), the voltage losses within the CL change drastically with N-modification. The combination of these two working conditions enables us to explain the outstanding performance of Pt/N-KB 600 as well as the improvement of Pt/N-KB 200, as a result of improved protonic pathway and reduced mass transport losses in the catalyst layer.

By comparing these two catalysts with Pt/N-KB 800, it was clear that the N-modification itself does not always lead to a more evenly distributed ionomer layer. Based on the physicochemical and electrochemical characterization of Pt/N-KB 800, it was also evident that the changes on the carbon support micro/mesoporous structure alone, which one might assume to be more favorable compared to the other two N-modified carbons, did not result in improvement of the mass transport resistance. This proves that observed carbon structural changes, due to ammonolysis at different temperatures, are not the main dominating factor in the change of the mass transport resistance.

We demonstrated that the nature of the N-functionalized carbon surface and their physico-chemical properties are important factors determining the support/ionomer interaction and hence increase performance. Ex-situ evaluation via XPS measurements showed a shift in the respective spectra N1s towards higher binding energies when ionomer was added to the carbon support. This proves the acid-base interaction between positively charged N-moieties and negatively charged ionomer $-SO_3^-$ groups. Even though all N modified carbon exhibited this interaction, the degree of this interaction and fraction of the N groups responsible for this, changed

with respect to the surface modification temperature. These interactions might be one factor resulting in a tailored solid/electrolyte interface which leads to a more homogenous ionomer distribution, which improves the local charge and mass transport conditions in a PEMFC. It was found that the MEA performance is directly correlated to the percentage of N-hydrogenation/protonation in the CL, which increases with higher fractions of pyrrolic/pyridinic groups within the carbon support. Nevertheless not the N-groups alone facilitate a homogeneous ionomer distribution. The catalyst layer performance and its configuration are of a very complex interplay between different parameter and catalyst properties. Thus the sum of all factors such as wettability, porosity, surface chemistry, ionomer distributing, ECSA, oxygen mass transport, proton pathways needs to be enhanced for improved MEA performance.

This work will serve as a stepping stone towards a better understanding and further improvement of carbon support modification concepts to tailor the ionomer configuration in the CL, which would, in turn, enable the development and manufacturing of new generations of MEAs.

Acknowledgments

This work was supported by the BMW Group. The authors would also like to thank the members of FC Test Field, FC Technology Development and Technology Material Analysis of BMW Group for their support during Fuel cell testing, MEA manufacturing and decal preparation. Special thanks goes to Steffen Hausdorf from TU Dresden for conducting water uptake measurements and the following fruitful discussions interpreting the results. Furthermore, M.L.L. acknowledges the financial support from the National Council of Science and Technology of Mexico (CONACyT, Grant 708585). This project received partial funding by the Bundesministerium für Bildung *u*nd Forschung (BMBF) via Project "KorrZellKat" (03XP0251) and by the Deutsche Forschungsgemeinschaft, (DFG, German Research Foundation) under Project STR 596/5-2 and STR 596/18-1.

ORCID

Peter Strasser https://orcid.org/0000-0002-3884-436X

References

1. O. Gröger, H. A. Gasteiger, and J. P. Suchsland, "Review—electromobility: batteries or fuel cells ?" *ECS*, **162**, A2605 (2015).
2. A. Kongkanand and M. F. Mathias, "The priority and challenge of high-power performance of low-platinum proton-exchange membrane fuel cells." *J. Phys. Chem. Lett.*, **7**, 1127 (2016).
3. Y.-C. Park, H. Tokiwa, K. Kakinuma, M. Watanabe, and M. Uchida, "Effects of carbon supports on Pt distribution, ionomer coverage and cathode performance for polymer electrolyte fuel cells." *J. Power Sources*, **315**, 179 (2016).
4. U.S. DRIVE Partnership, U.S. DRIVE (Driving Research andInnovation for Vehicle efficiency and Energy sustainability) (2018), https://energy.gov/sites/prod/files/2014/02/f8/fctt_roadmap_june2013.pdf.
5. A. Orfanidi, P. Madkikar, H. A. El-Sayed, G. S. Harzer, T. Kratky, and H. A. Gasteiger, "The key to high performance low pt loaded electrodes." *J. Electrochem. Soc.*, **164**, F418 (2017).
6. A. Ohma, T. Mashio, K. Sato, H. Iden, Y. Ono, K. Sakai, K. Akizuki, S. Takaichi, and K. Shinohara, "Analysis of proton exchange membrane fuel cell catalyst layers for reduction of platinum loading at nissan." *Electrochim. Acta*, **56**, 10832 (2011).
7. V. Yarlagadda, M. K. Carpenter, T. E. Moylan, R. S. Kukreja, R. Koestner, W. Gu, L. Thompson, and A. Kongkanand, "Boosting fuel cell performance with accessible carbon mesopores." *ACS Energy Lett.*, **3**, 618 (2018).
8. A. Z. Weber and A. Kusoglu, "Unexplained transport resistances for low-loaded fuel-cell catalyst layers." *J. Mater. Chem. A*, **2**, 17207 (2014).
9. G. S. Harzer, A. Orfanidi, H. El-Sayed, P. Madkikar, and H. A. Gasteiger, "Tailoring catalyst morphology towards high performance for low Pt loaded PEMFC cathodes." *J. Electrochem. Soc.*, **165**, F770 (2018).
10. N. Ramaswamy, W. Gu, J. M. Ziegelbauer, and S. Kumaraguru, "Carbon support microstructure impact on high current density transport resistances in PEMFC cathode." *ECS*, **167**, 064515 (2020).
11. A. Orfanidi, P. J. Rheinlander, N. Schulte, and H. A. Gasteiger, "Ink solvent dependence of the ionomer distribution in the catalyst layer of a PEMFC." *J. Electrochem. Soc.*, **165**, F1254 (2018).
12. L. Pan, S. Ott, F. Dionigi, and P. Strasser, "Current challenges related to the deployment of shape-controlled Pt alloy oxygen reduction reaction nanocatalysts into low Pt-loaded cathode layers of proton exchange membrane fuel cells." *Current Opinion in Electrochemistry*, **18**, 61 (2019).
13. F. Dionigi et al., "Controlling near-surface Ni composition in octahedral PtNi(Mo) nanoparticles by Mo doping for a highly active oxygen reduction reaction catalyst." *Nano Lett.*, **19**, 6876 (2019).
14. L. Chong, J. Wen, J. Kubal, F. G. Sen, J. Zou, J. Greeley, M. Chan, H. Barkholtz, W. Ding, and D.-J. Liu, "Ultralow-loading platinum-cobalt fuel cell catalysts derived from imidazolate frameworks." *Science*, **362**, 1276 (2018).
15. X. Huang et al., "High-performance transition metal–doped Pt3Ni octahedra for oxygen reduction reaction." *Science*, **348**, 1230 (2015).
16. S. Ott, A. Orfanidi, H. Schmies, B. Anke, H. N. Nong, J. Hubner, U. Gernert, M. Gliech, M. Lerch, and P. Strasser, "Ionomer distribution control in porous carbon-supported catalyst layers for high-power and low Pt-loaded proton exchange membrane fuel cells." *Nat. Mater.*, **19**, 77 (2020).
17. F. Yang, L. Xin, A. Uzunoglu, Y. Qiu, L. Stanciu, J. Ilavsky, W. Li, and J. Xie, "Investigation of the interaction between nafion ionomer and surface functionalized carbon black using both ultrasmall angle X-ray scattering and cryo-TEM." *ACS Appl. Mater. Interfaces*, **9**, 6530 (2017).
18. L. Xin, Y. Kang, F. Yang, A. Uzunoglu, T. Rockward, P. J. Ferreira, R. L. Borup, J. Ilavsky, L. Stanciu, and J. Xie, *Paper presented at the ECS Conference*, Hawai (2016).
19. S. Ott, F. Du, M. L. Luna, T. A. Dao, S. Selve, B. R. Cuenya, A. Orfanidi, and P. Strasser, "Property-reactivity relations of N-doped PEM fuel cell cathode catalyst supports." *Appl. Catalysis B*, **306**, 121118 (2022).
20. K. Kodama, K. Motobayashi, A. Shinohara, N. Hasegawa, K. Kudo, R. Jinnouchi, M. Osawa, and Y. Morimoto, "Effect of the side-chain structure of perfluorosulfonic acid ionomers on the oxygen reduction reaction on the surface of Pt." *ACS Catal.*, **8**, 694 (2017).
21. V. C. Yarlagadda et al., "Boosting fuel cell performance with accessible carbon mesopores." *ACS Energy Lett.*, **3**, 618 (2018).
22. S. Ott, A. Bauer, F. Du, T. A. Dao, M. Klingenhof, A. Orfanidi, and P. Strasser, "Impact of carbon support meso-porosity on mass transport and performance of PEMFC cathode catalyst layers." *ChemCatChem*, **13**, 4759 (2021).
23. M. B. Sassin, Y. Garsany, R. W. Atkinson, R. M. E. Hjelm, and K. E. Swider-Lyons, "Understanding the interplay between cathode catalyst layer porosity and thickness on transport limitations en route to high-performance PEMFCs." *Int. J. Hydrogen Energy*, **44**, 16944 (2019).
24. Y.-C. Park, K. Kakinuma, H. Uchida, M. Watanabe, and M. Uchida, "Effects of short-side-chain perfluorosulfonic acid ionomers as binders on the performance of low Pt loading fuel cell cathodes." *J. Power Sources*, **275**, 384 (2015).
25. K. Artyushkova, M. J. Workman, I. Matanovic, M. J. Dzara, C. Ngo, S. Pylypenko, A. Serov, and P. Atanassov, "Role of surface chemistry on catalyst/ionomer interactions for transition metal–nitrogen–carbon electrocatalysts." *ACS Appl. Energy Mater.*, **1**, 68 (2017).
26. J. Landers, G. Y. Gor, and A. V. Neimark, "Density functional theory methods for characterization of porous materials." *Colloids Surf., A*, **437**, 3 (2013).
27. G. Y. Gor, M. Thommes, K. A. Cychosz, and A. V. Neimark, "Quenched solid density functional theory method for characterization of mesoporous carbons by nitrogen adsorption." *Carbon*, **50**, 1583 (2012).
28. A. V. Neimark, Y. Lin, P. I. Ravikovitch, and M. Thommes, "Quenched solid density functional theory and pore size analysis of micro-mesoporous carbons." *Carbon*, **47**, 1617 (2009).
29. I. J. L. Yeh, "I., Atomic subshell photoionization cross sections and asymmetry parameters." *At. Data Nucl. Data Tables*, **32**, 1 (1985).
30. K. Artyushkova, "Misconceptions in interpretation of nitrogen chemistry from X-ray photoelectron spectra." *Journal of Vacuum Science & Technology A*, **38**, 031002 (2020).
31. K. F. Ortega, R. Arrigo, B. Frank, R. Schlögl, and A. Trunschke, "Acid–base properties of N-doped carbon nanotubes: a combined temperature-programmed desorption, X-ray photoelectron spectroscopy, and 2-propanol reaction investigation." *Chem. Mater.*, **28**, 6826 (2016).
32. F. Späth, W. Zhao, C. Gleichweit, K. Gotterbarm, U. Bauer, O. Höfert, H. P. Steinrück, and C. Papp, "Hydrogenation and dehydrogenation of nitrogen-doped graphene investigated by X-ray photoelectron spectroscopy." *Surf. Sci.*, **634**, 89 (2015).
33. R. Arrigo, M. Hävecker, R. Schlögl, and D. S. Su, "Dynamic surface rearrangement and thermal stability of nitrogen functional groups on carbon nanotubes." *Chem. Comm.*, **40**, 4891 (2008).
34. I. Matanovic, K. Artyushkova, M. B. Strand, M. J. Dzara, S. Pylypenko, and P. Atanassov, "Core level shifts of hydrogenated pyridinic and pyrrolic nitrogen in the nitrogen-containing graphene-based electrocatalysts: in-plane vs edge defects." *The Journal of Physical Chemistry C*, **120**, 29225 (2016).
35. K. Shinozaki, Y. Morimoto, B. S. Pivovar, and S. S. Kocha, "Suppression of oxygen reduction reaction activity on Pt-based electrocatalysts from ionomer incorporation." *J. Power Sources*, **325**, 745 (2016).
36. R. B. Baker, D. A. Caulk, K. C. Neyerlin, and M. W. Murph, "Measurement of oxygen transport resistance in pem fuel cells by limiting current methods." *J. Electrochem. Soc.*, **156**, B991 (2009).
37. F. Du et al., "Effects of PEMFC operational history under dry/wet conditions on additional voltage losses due to ionomer migration." *J. Electrochem. Soc.*, **167**, 144513 (2020).
38. G. Tsotridis, A. Pilenga, G. D. Marco, and T. Malkow, "EU harmonised test protocols for PEMFC MEA testing in single cell confoguration for automotive applications." *JRC Science Hub* (2015).

39. S. K. Jomori, K. N. Nonoyama, M. Kato, and T. Yoshida, "An experimental study of the effects of operational history on activity changes in a PEMFC." *J. Electrochem. Soc.*, **160**, F1073 (2013).
40. Y. Liu, C. Ji, W. Gu, J. Jorne, and H. A. Gasteiger, "Effects of catalyst carbon support on proton conduction and cathode performance in PEM." *Fuel Cells. ECS*, **158**, B614 (2011).
41. X. Li, H. Wang, J. T. Robinson, H. Sanchez, G. Diankov, and H. Dai, "Simultaneous nitrogen doping and reduction of graphene oxide." *JACS*, **43**, 15939 (2009).
42. R. P. Rocha, O. S. G. P. Soares, A. G. Gonçalves, J. J. M. Órfão, M. F. R. Pereira, and J. L. Figueiredo, "Different methodologies for synthesis of nitrogen doped carbon nanotubes and their use in catalytic wet air oxidation." *Appl. Catal., A*, **548**, 62 (2017).
43. B. Zhang, Z. Wen, S. Ci, S. Mao, J. Chen, and Z. He, "Synthesizing nitrogen-doped activated carbon and probing its active sites for oxygen reduction reaction in microbial fuel cells." *ACS Appl. Mater. Interfaces*, **6**, 7464 (2014).
44. R. Arrigo, M. Havecker, R. Schlogl, and D. S. Su, "Dynamic surface rearrangement and thermal stability of nitrogen functional groups on carbon nanotubes." *Chem Commun (Camb)*, **40**, 4891 (2008).
45. S. Chae, G. Panomsuwan, M. A. Bratescu, K. Teshima, and N. Saito, "p-Type doping of graphene with cationic nitrogen." *ACS Appl. Nano Mater.*, **2**, 1350 (2019).
46. S. Rojas-Carbonell, K. Artyushkova, A. Serov, C. Santoro, I. Matanovic, and P. Atanassov, "Effect of pH on the activity of platinum group metal-free catalysts in oxygen reduction reaction." *ACS Catal.*, **8**, 3041 (2018).
47. M. Toupin and D. Be´langer, "Spontaneous Functionalization of carbon black by reaction with 4-nitrophenyldiazonium cations." *Langmuir*, **24**, 1910 (2008).
48. D. R. Baker, C. A. Caulk, K. C. Neyerlin, and M. W. Murph, "Measurement of oxygen transport resistance in PEM fuel cells by limiting current methods." *J. Electrochem. Soc.*, **156**, B991 (2009).
49. H. Oha, Y.-i Leea, G. Leea, K. Mina, and J. S. Yi, "Experimental dissection of oxygen transport resistance in thecomponents of a polymer electrolyte membrane fuel cell." *ECS*, **345**, 67 (2017).
50. R. Jinnouchi, K. Kudo, N. Kitano, and Y. Morimoto, "Molecular dynamics simulations on O_2 permeation through nafion ionomer on platinum surface." *Electrochim. Acta*, **188**, 767 (2016).
51. C. Zhan, Y. Zhang, P. T. Cummings, and D. E. Jiang, "Enhancing graphene capacitance by nitrogen: effects of doping configuration and concentration." *Phys. Chem. Chem. Phys.*, **18**, 4668 (2016).
52. S. M. Li, S. Y. Yang, Y.-S. Wang, H.-P. Tsai, H.-W. Tien, S. T. Hsiao, W.-H. Liao, C.-L. Chang, C.-C. M. Ma, and C.-C. Hu, "N-doped structures and surface functional groups of reduced graphene oxide and their effect on the electrochemical performance of supercapacitor with organic electrolyte." *J. Power Sources*, **278**, 218 (2015).
53. M. K. Hoque, J. A. Behan, S. N. Stamatin, F. Zen, T. S. Perova, and P. E. Colavita, "Capacitive storage at nitrogen doped amorphous carbon electrodes: structural and chemical effects of nitrogen incorporation." *RSC Adv.*, **9**, 4063 (2019).
54. H. M. Jeong, J. W. Lee, W. H. Shin, Y. J. Choi, H. J. Shin, J. K. Kang, and J. W. Choi, "Nitrogen-doped graphene for high-performance ultracapacitors and the importance of nitrogen-doped sites at basal planes." *Nano Lett.*, **11**, 2472 (2011).
55. J.-I. Kim and S.-J. Park, "Effect of nitrogen-containing groups on enhanced capacitive behaviors of multi-walled carbon nanotubes." *J. Solid State Chem.*, **184**, 2184 (2011).
56. D. S. Jeong, J. M. Yun, and K.-H. Kim, "Highly porous nitrogen-doped carbon for superior electric double-layer capacitors." *RSC Adv.*, **7**, 44735 (2017).
57. W. Li, D. Chen, Z. Li, Y. Shi, Y. Wan, G. Wang, Z. Jiang, and D. Zhao, "Nitrogen-containing carbon spheres with very large uniform mesopores: The superior electrode materials for EDLC in organic electrolyte." *Carbon*, **45**, 1757 (2007).
58. G. Lota, B. Grzyb, H. Machnikowska, J. Machnikowski, and E. Frackowiak, "Effect of nitrogen in carbon electrode on the supercapacitor performance." *Chem. Phys. Lett.*, **404**, 53 (2005).
59. R. K. Blundell, "P. Licence, Quaternary ammonium and phosphonium based ionic liquids: a comparison of common anions." *Phys. Chem. Chem. Phys.*, **16**, 15278 (2014).
60. A. R. Santos, R. K. Blundell, and P. Licence, "XPS of guanidinium ionic liquids: a comparison of charge distribution in nitrogenous cations." *Phys. Chem. Chem. Phys.*, **17**, 11839 (2015).
61. K. Zeng and Z.-X. Cao, "Protonation of pyrrole and furan by H_3O^+ and NH^{4+} in the gas phase: a density functional theory study." *Chin. J. Chem.*, **24**, 293 (2006).
62. U. I. Kramm, I. Herrmann-Geppert, J. Behrends, K. Lips, S. Fiechter, and P. Bogdanoff, "On an easy way to prepare metal-nitrogen doped carbon with exclusive presence of MeN_4-type sites active for the ORR." *J. Am. Chem. Soc.*, **138**, 635 (2016).
63. K. Artyushkova, B. Kiefer, B. Halevi, A. Knop-Gericke, R. Schlogl, and P. Atanassov, "Density functional theory calculations of XPS binding energy shift for nitrogen-containing graphene-like structures." *Chem Commun (Camb)*, **49**, 2539 (2013).
64. S. Kabir, K. Artyushkova, A. Serov, B. Kiefer, and P. Atanassov, "Binding energy shifts for nitrogen-containing graphene-based electrocatalysts - experiments and DFT calculations." *Surf. Interface Anal.*, **48**, 293 (2016).